A&A, 707, A122 (2026)
https://doi.org/10.1051/0004-6361/202556053

Astronomy & Astrophysics

X-ray emission in IllustrisTNG circum-cluster environments

II. Possible origins of the soft X-ray excess emission

Celine Gouin[1,⋆], Daniela Galárraga-Espinosa[2,3], Massimiliano Bonamente[4], Stephen Walker[4], Mohammad Mirakhor[4], Richard Lieu[4], Clotilde Laigle[1], Etienne Bonnassieux[5], Charlotte Welker[6], Stefano Gallo[7], Tony Bonnaire[8], and Jade Paste[1]

[1] Sorbonne Université, UMR7095, Institut d'Astrophysique de Paris, 98 bis Boulevard Arago, 75014 Paris, France
[2] Max-Planck Institute for Astrophysics, Karl-Schwarzschild-Str. 1, D-85741 Garching, Germany
[3] Kavli IPMU (WPI), UTIAS, The University of Tokyo, Kashiwa Chiba 277-8583, Japan
[4] University of Alabama in Huntsville, Department of Physics and Astronomy, Huntsville, AL 35899, USA
[5] Instituto de Astrofísica de Andalucía, Consejo Superior de Investigaciones Científicas (CSIC), Glorieta de la Astronomía s/n, E-18008 Granada, Spain
[6] New York City College of Technology, City University of New York, Physics Department, Brooklyn, NY, USA
[7] Université Paris-Saclay, CNRS, Institut d'Astrophysique Spatiale, 91405 Orsay, France
[8] Laboratoire de Physique de l'Ecole Normale Supérieure, ENS, Université PSL, CNRS, Sorbonne Université, Université Paris Cité, F-75005 Paris, France

Received 23 June 2025 / Accepted 10 January 2026

ABSTRACT

Context. An excess of soft X–ray emission (~0.2−1 keV) above the contribution from the hot intracluster medium (ICM) has been detected in a number of galaxy clusters, including the Coma cluster. The physical origin of this emitting medium above the hot ICM has not yet been determined, in particular, it is unclear whether it is thermal or nonthermal.
Aims. We investigate the gas phase and gas structure that reproduce the soft excess radiation from the cluster core to the outskirts best using simulations.
Method. By using the IllustrisTNG simulation (TNG300), we predict the radial profile of thermodynamic properties and the soft X–ray surface brightness of 138 clusters within $5 \times r_{200}$. Their X–ray emission was simulated for the hot ICM gas phase ($T \geq 10^7$ K), the entire warm–hot medium at a temperature $T = 10^{5-7} K$ (WARM), and for the diffuse and low–density warm–hot intergalactic medium (WHIM).
Results. The soft excess inside clusters appears to be produced by substructures of the WARM gas phase that host dense warm clumps, that is, the warm circumgalactic medium (WCGM), and the inner soft excess is strongly correlated with substructure and the WCGM mass fractions. Outside of the virial radius, the fraction of WHIM gas that is mostly inside filaments that are connected to clusters boosts the soft X–ray excess. The more diffuse the gas, the higher the soft X-ray excess beyond the virial region.
Conclusion. The thermal emission of the WARM gas phase in the form of WCGM clumps and WHIM diffuse filaments reproduces the soft excess emission that was observed up to the virial radius in Coma and in the inner regions of other massive clusters. Moreover, our analysis suggests that soft X–ray excess is a proxy of the dynamical cluster state and that higher excess is observed in the most unrelaxed clusters.

Key words. methods: numerical – methods: statistical – galaxies: clusters: general – galaxies: clusters: intracluster medium – X-rays: galaxies: clusters

1. Introduction

A hot and diffuse intracluster medium (ICM) is the dominant reservoir of baryonic matter in galaxy clusters, with a typical mass fraction ($f_{\rm gas}$) of 10–20% of the total mass that is required to keep the hot gas in hydrostatic equilibrium with an unseen dark matter component (e.g. Allen et al. 2004; Landry et al. 2013; Mantz et al. 2022). With typical temperatures of $\log_{10} T(\mathrm{K}) \geq 7$ (e.g. Leccardi & Molendi 2008), the hot ICM is readily observable with imaging X–ray detectors, especially at photon energies $\gtrsim$1 keV, where the interstellar medium (ISM) Galactic absorption is less significant (e.g. Dickey & Lockman 1990; Kalberla et al. 2005; HI4PI Collaboration 2016).

At large scales, different gas phases dominate different cosmic web environments, according to cosmological hydrodynamical simulations (Martizzi et al. 2019). In general, the densest structures such as the cluster cores are mainly in the form of hot plasma. In contrast, filaments and sheets are mostly populated by warm gas, and voids are dominated by cold gas in the form of the intergalactic medium (IGM). Matter flows from filaments to clusters in the large-scale filamentary network (Hahn et al. 2015). In this context, hydrodynamical cosmological simulations are our best option for understanding the physics of this gas that is accreted from filaments to clusters. Numerous physical processes are thus explored in state-of-the-art simulations, such as the turbulence induced by large cosmic flow (Vallés-Pérez et al. 2021; Mohapatra et al. 2022), merging events and accretion shocks (see e.g. Shi et al. 2020),

⋆ Corresponding author: gouin@iap.fr

the presence of cool-core (Braspenning et al. 2024), and the dependence on baryonic physic models, such as Active Galactic Nuclei (AGN) feedback, in pushing out gas from cluster centers (Hahn et al. 2017).

Numerous physical processes are thus explored in advanced simulations, such as the turbulence induced by large cosmic flow (Vallés-Pérez et al. 2021; Mohapatra et al. 2022), merging events (see e.g. Shi et al. 2020), and the presence of cool core (Braspenning et al. 2024). In addition, the dependence on baryonic physic models, such as Active Galactic Nuclei (AGN) feedback, is also affecting the gas distribution, in pushing out the gas from cluster centers (Hahn et al. 2017). In particular, by using the recent results from eROSITA, Bahar et al. (2024) have recently attempted to constrain AGN feedback from the X-ray emission of groups. Recently, Shreeram et al. (2025a) have proposed a novel forward model to constrain the AGN X-ray luminosity jointly with the radial hot-gas distribution based mock X-ray emission from IllustrisTNG simulation (Shreeram et al. 2025b).

At soft X-ray energies (∼0.1–1 keV), some clusters show an excess of soft X-ray emission within the virial radius. This is defined as an excess of counts above the expected soft X-ray emission from the hot ICM gas as modeled from its harder X-ray emissions. This soft excess was first observed in Extreme Ultraviolet Explorer (EUVE) observations of the Coma and Virgo clusters (Lieu et al. 1996b,a; Bowyer et al. 1996) and was later observed by ROSAT in different clusters (Bonamente et al. 2001a,b, 2002). This excess was also observed by X-ray Multi-Mirror Mission (XMM–Newton) (e.g. Nevalainen et al. 2003; Kaastra et al. 2003; Bonamente et al. 2005), Beppo-SAX (Bonamente et al. 2001c), and even by Chandra (Bonamente & Nevalainen 2011). Measurements of the soft excess in particular rely on the accuracy of (a) the estimate of the hot ICM contribution to the soft band, (b) the background subtraction, and (c) the effect of the foreground Galactic absorption, which varies in time and space (e.g. Snowden et al. 1994, 1995). Although some of the detections have been questioned or revised based on the uncertainties on these aspects of the data analysis (e.g. Bowyer et al. 1999; Nevalainen et al. 2007; Bonamente & Nevalainen 2011), the soft excess is now an established observational feature of some galaxy clusters. In particular, we focus on the comparison with the strong soft excess out to the virial radius for the Coma cluster, which is one of the most massive and nearby clusters (Bonamente et al. 2003, 2009; Mirakhor & Walker 2020; Bonamente et al. 2022).

The interpretation of this soft excess has so far been elusive because it has not been possible to confirm emission lines associated with the excess with a high statistical probability (as reported by Kaastra et al. 2003; Finoguenov et al. 2003) because the resolution of the X–ray instruments is limited. It is unclear whether the soft excess originates from within the virial cluster radius (e.g., as originally investigated by Cheng et al. 2005) or from external filaments that are projected against the cluster (e.g., as investigated in Churazov et al. 2023b). It is therefore of interest to study the properties of the baryonic phases within the virial radius, where the hot gas is the dominant baryonic form, and in its immediate vicinity, where warm subvirial gas is still accreting toward clusters and is expected to be densest and therefore more readily observable.

In Gouin et al. (2023) (hereafter Paper I), we began to investigate the gas properties and soft X-ray emission in the circumcluster environment, which is defined as the region within a few virial radii of galaxy clusters, using the IllustrisTNG simulation (Pillepich et al. 2018; Nelson et al. 2019). In this follow-up paper, we focus on the origin of the soft X–ray emission and on its dependence on the gas properties. This paper is structured as follows. We describe in Sect. 2 the numerical methods we used to predict soft X–ray emission in the circumcluster environment. In Sect. 3 we compare the soft X–ray predictions to current observations and discuss the detectability of warm gas. In Sect. 4 we investigate the possible origin of this soft excess as a function of the gas properties and gas structures. In Sect. 5 we discuss our results in the context of recent observations and predictions, and we present our conclusions in Sect. 6.

2. Numerical predictions of the soft X–ray emission

The IllustrisTNG simulation and the analysis methods used for this project were presented in Gouin et al. (2023), and they are briefly summarized here. We used the TNG300-1 simulation at $z = 0$, which is the largest volume (∼300 Mpc^3) in the IllustrisTNG suite with the highest spatial resolution. This provides a statistically significant cluster sample and enabled us to model the baryonic physics in detail (Pillepich et al. 2018; Nelson et al. 2019). We divided the baryons into different phases as defined in Table 1: the hot ICM at $\log T(\mathrm{K}) \geq 7$, and the warm gas at $5 \leq \log T(\mathrm{K}) \leq 7$ (WARM), which is further subdivided into the denser warm–hot circumgalactic medium (WCGM) at $n_e \geq 10^{-4}$ cm^{-3} and the diffuser warm–hot intergalactic medium (WHIM) at lower density, which is typically found in filaments (see e.g. Galárraga-Espinosa et al. 2021; Gouin et al. 2022). Thermodynamic quantities of interest such as the density, temperature, chemical abundance, and clumpiness of the gas were averaged in spherical shells out to $5 \times r_{200}$, which is the outermost radius we considered. As explained in Paper I, we did not compute the thermodynamic profiles (and thus, the soft X–ray emission) of the WCGM gas alone because there are not enough particles from which we might obtain smooth profiles because their distribution fluctuates strongly. Instead of the WCGM phase alone, we combined the WCGM and WHIM gas into the WARM gas phase to explore the soft X–ray emission of the diffuse (WHIM) and clumpy (WCGM) warm gas, in contrast to the hot ICM. Our sample of 138 clusters was divided into three subsets ordered by increasing mass, as shown in Table 2, as we did in Paper I.

2.1. Thermodynamic quantities

We begin by summarizing the gas profiles for the two dominant gas phases in the cluster environment, the hot ICM and the WARM gas. These two phases are necessary to simulate the X-ray emission because they are the two dominant gas phases in the circumcluster environments (Martizzi et al. 2019; Gouin et al. 2022). The method for computing the radial profiles of the thermodynamic properties is detailed in Paper I, and it is summarized here. For each cluster, we computed the radial profiles of the thermodynamic quantities within spherical shells centered on the cluster, and the cluster-centric distance was normalized by r_{200}. Each profile was obtained by averaging over the gas cells of a given phase using a volume-weighted average for each gas cell. For the temperature, we tested three different weights, the cell volume, the mass, and the emissivity -weighted average. We concluded that they do not affect our results significantly. Moreover, we corrected the metallically profile by a factor 1.6 following Vogelsberger et al. (2018). These authors found that the TNG300-1 metallicity profiles should be shifted by a factor of 1.6 to match the highly resolved TNG100-1 simulations.

Table 1. Definition of the gas phases. The WARM gas is the sum of the WHIM and WCGM gas phases.

Gas phase	Density [cm^{-3}]	Temperature [K]	Environments
HOT gas	–	$T > 10^7$	Dominant inside cluster ($r < r_{200}$), referred as hot ICM
WARM gas	–	$10^5 < T < 10^7$	Dominant outside cluster ($r > r_{200}$)
WHIM gas	$n_e < 10^{-4}$ cm^{-3}	$10^5 < T < 10^7$	Dominant inside filaments (Galárraga-Espinosa et al. 2021)
WCGM gas	$n_e \geq 10^{-4}$ cm^{-3}	$10^5 < T < 10^7$	Clumps of gas tracing filaments (Angelinelli et al. 2021)

Table 2. Main properties of the entire cluster sample and its four mass bins M_1, M_2, M_3, and M_4. Sample M_4 is also included in M_3. Sample M_4 is composed of the five most massive clusters and represents a Coma-like cluster sample.

Sample	Mass range	$\langle M_{200} \rangle$	$\langle r_{200} \rangle$	Number of clusters
All clusters	$\log(M_{200}[M_\odot/h]) > 14$	$1.97 \times 10^{14}\ M_\odot/h$	$0.92/h$ Mpc	138
M_1	$14.0 < \log(M_{200}[M_\odot/h]) < 14.1$	$1.13 \times 10^{14}\ M_\odot/h$	$0.78/h$ Mpc	47
M_2	$14.1 < \log(M_{200}[M_\odot/h]) < 14.5$	$1.91 \times 10^{14}\ M_\odot/h$	$0.92/h$ Mpc	78
M_3	$\log(M_{200}[M_\odot/h]) > 14.5$	$5.37 \times 10^{14}\ M_\odot/h$	$1.3/h$ Mpc	13
M_4	$\log(M_{200}[M_\odot/h]) > 14.75$	$7.61 \times 10^{14}\ M_\odot/h$	$1.5/h$ Mpc	5

This discrepancy was also found in Cluster-EAGLE clusters by Barnes et al. (2017).

Figure 1 illustrates the averaged radial profiles of the gas density, temperature, and metal abundance for our three main cluster mass bins. The top left panel displays the mean density within spherical radial shells centered on the clusters. We found that the radial density of the WARM gas is significantly affected by the cluster mass. Compared to high-mass clusters, low-mass clusters contain denser WARM gas within approximately the virial radius, and the behavior beyond it is different. The radius at which the WARM density becomes higher than the HOT gas density occurs at about $r = 0.9\ r_{200}$ for M_1, at $1.3\ r_{200}$ for M_2, and at $2.1\ r_{200}$ for M_3. This shows that the hot ICM dominates the cluster region out to larger radii for more massive clusters. The top right panel shows that the WARM temperature does not depend on the cluster mass, unlike for the hot ICM gas. As expected and well established observationally, clusters with higher masses have hotter ICM temperatures than lower mass clusters because their gravitational wells are deeper. This also naturally accounts for the faster transition from HOT to WARM in lower-mass clusters. The metal abundance in the WARM gas in the bottom left panel is significantly higher than in the ICM. The radial gradient starts from near solar levels at the center and decreases to approximately 10% solar at the virial radius. Beyond this radius, the abundance in the WARM phase is subsolar. The metallicity profile agrees with findings from the TNG-Cluster Simulation (Nelson et al. 2024), which indicated a minor sensitivity to the halo mass and achieved about $0.4\ Z_\odot$ in the cluster centers. Comparisons between our simulated density, temperature, and metallicity profiles and the observations and other simulations were presented in Paper I. The results agreed well.

The X–ray surface brightness is proportional to the square of the density. It is thus highly sensitive to inhomogeneities in the emitting phases. The radial profiles of the clumpiness factor of the various phases is defined as

$$C = \frac{\langle n^2 \rangle}{\langle n \rangle^2}, \tag{1}$$

with n the gas density (see Nagai & Lau 2011, for a definition). The bottom right panel of Fig. 1 shows the clumpiness profile of the HOT and WARM gas. The WARM gas is substantially more clumpy than the hot ICM within and beyond the virial radius and for all cluster mass bins. Moreover, the clumping of the WARM gas and the cluster mass beyond $0.5 \times r_{200}$ is strongly correlated, such that more massive clusters have clumpier WARM gas around them. The clumpiness of the gas plays a crucial role when the subsequent X–ray emission is investigated. We show below that the clumpier the WARM gas, the higher the soft X–ray excess. Equivalent clumpiness measurements, along with comparisons between our analysis, observations, and other simulations, were also presented in Paper I.

2.2. Masses and gas-mass fractions

The mass of the various gas phases was obtained as a straightforward integration of the density profiles of Fig. 1. An estimate of the total mass implied by the assumption of hydrostatic equilibrium (HSE) can be also calculated (as shown in Paper I). In this paper, we instead focus on the relative ratios of the baryonic masses, and we do not discuss hydrostatic masses.

Figure 2 shows the radial profiles of the integrated ICM, WARM, and WHIM gas masses (top panel) as a function of cluster mass. In the bottom panels, we illustrate the mass ratios of WARM to HOT, WHIM to HOT, and WCGM to HOT, computed as integrated gas-mass profiles. This analysis of the IllustrisTNG simulation provides a number of useful clues as to the locations of baryons in circumcluster environments. We list these clues below.

- In the inner cluster regions ($r \leq 0.5 \times r_{200}$), only lower–mass clusters have a significant amount of WARM gas. It is at a level of ~0.1–1% of the hot ICM. This WARM gas is in the WCGM gas phase, as expected previously from the high density of the WARM gas inside these low-mass clusters.
- Near the virial radius, most of the WARM gas in lower–mass clusters is in the form of diffuse WHIM gas, while high–mass clusters have comparable WCGM and WHIM gas masses. This is expected from the radial extension in the ICM of higher–mass clusters, which are located relatively farther away from their center than lower–mass clusters.
- Interestingly, clusters appear to have a constant radius of about $2 \times r_{200}$ whithin which the WARM gas mass is

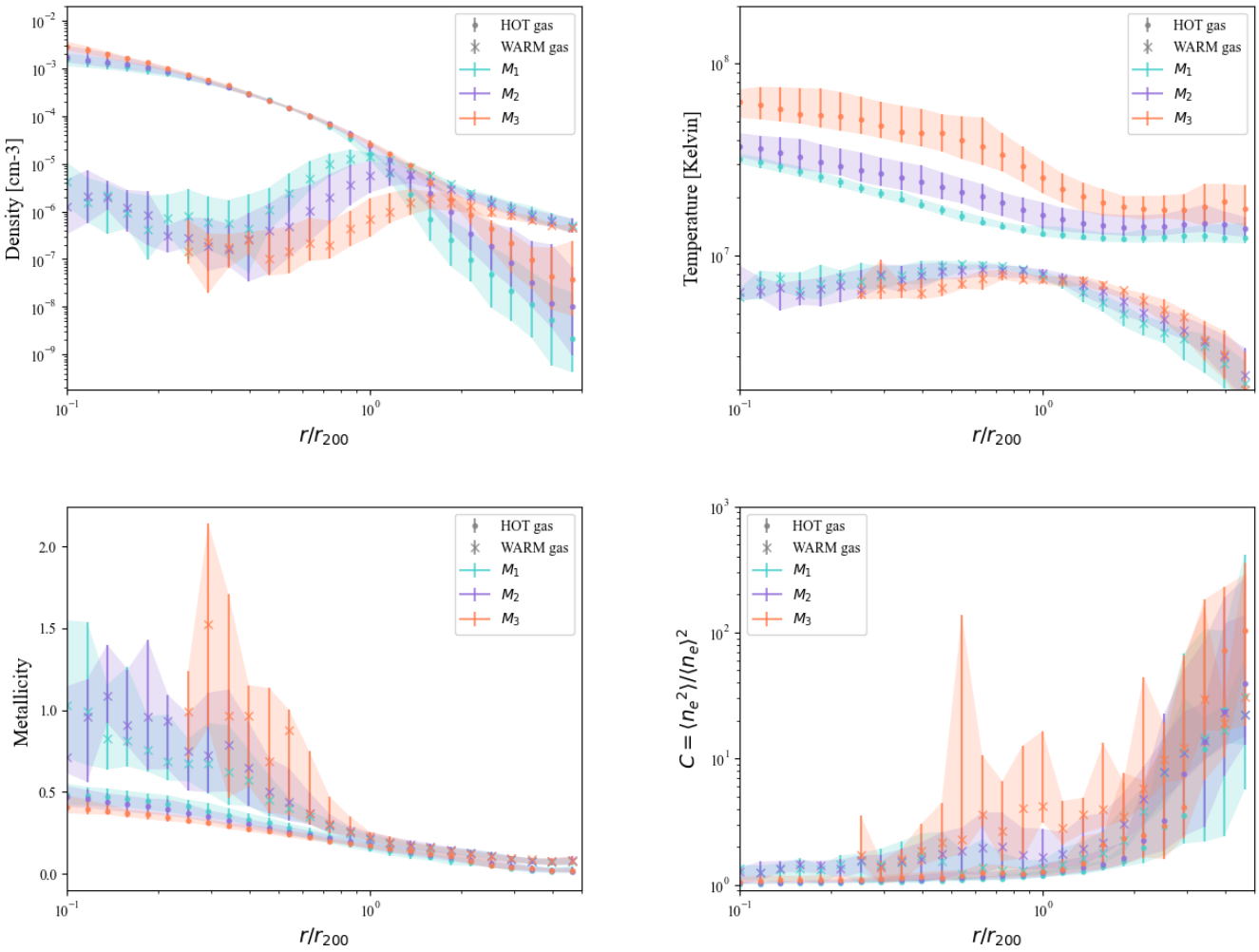

Fig. 1. Median radial profile of the gas properties for the two main gas phases (HOT and WARM gas, as defined in Table 1) as a function of the mass bins M_1, M_2, and M_3, plotted in blue, purple, and orange, respectively (as defined in Table 2). The error bars are the percentiles from 20% to 80%. The average density (top left), temperature (top right), metal abundance (bottom left), and clumpiness (bottom right) profiles are illustrated in the different panels.

approximately 2×10^{13} $M_\odot$, regardless of the cluster mass. Beyond this radius, the WARM mass increases in proportion to the cluster mass, as expected. At these large radii ($r > 2 \times r_{200}$), almost all the WARM gas is in the form of diffuse WHIM, whereas the WCGM clumps represent only about 5% of the WARM gas mass.

2.3. The X–ray surface brightness

The X–ray surface brightness is defined as

$$S_X(\theta) = \frac{1}{4\pi(1+z)^4} \int_l n_e n_H \Lambda(T, A)\, \mathrm{d}l(\theta), \tag{2}$$

and it is given in units of [erg cm^{-2} s^{-1} Srad^{-1}]. The radiation is assumed to be isotropic by the 4π factor (see Eq. 5 of Paper I). In Eq. (2), $\Lambda(T, A)$ is the emissivity of the plasma, calculated in [keV s^{-1} cm^3] with the software `pyAtomDB`, as shown in Paper I, and it is a function of the average plasma temperature and abundance. n_e and n_H are the electron and hydrogen number density in [cm^{-3}], respectively, and the integration is made along the sightline at a give projected radial distance θ. The X–ray surface brightness is also known as the intensity of the radiation I, or of the energy emitted per unit time, solid angle, and detector area perpendicular to the radiation. The intensity is a convenient astrophysical quantity because it is a quantity that is (nearly) independent of distance or redshift because the solid angle of the emitted radiation and the surface area of the detector scale in opposite ways with the distance between the detector and the source (e.g. Rybicki & Lightman 1979). Because the radiation is optically thin, the surface brightness was obtained as an integration along the sightline at a constant projected angular distance θ of $n_e n_H \Lambda(T, A)$ in 50 radial bins between 0.05 and $5 \times r_{200}$, which correspond to the same number of cylindrical shells, as described in detail in Paper I, where details of the projection of the 3D radial profiles (e.g., Fig. 1) were discussed. In particular, the use of these azymuthally symmetric 3D radial profiles means that the effect of triaxial geometry is accounted for in the projection in the sample sense because there is no choice of a specific axis over which the projection is made.

Considering this formalism, we used the thermodynamic radial profiles of each cluster to predict its associated X–ray surface brightness profile. Figure 3 shows the average surface brightness profiles for our three cluster mass ranges considering an X–ray band of 0.2-0.4 keV. The results and their interpretation are very similar for the second soft X–ray band of interest (0.2-1 keV), and this band is not shown in the figure. We highlight the relative importance of the X–ray surface brightness

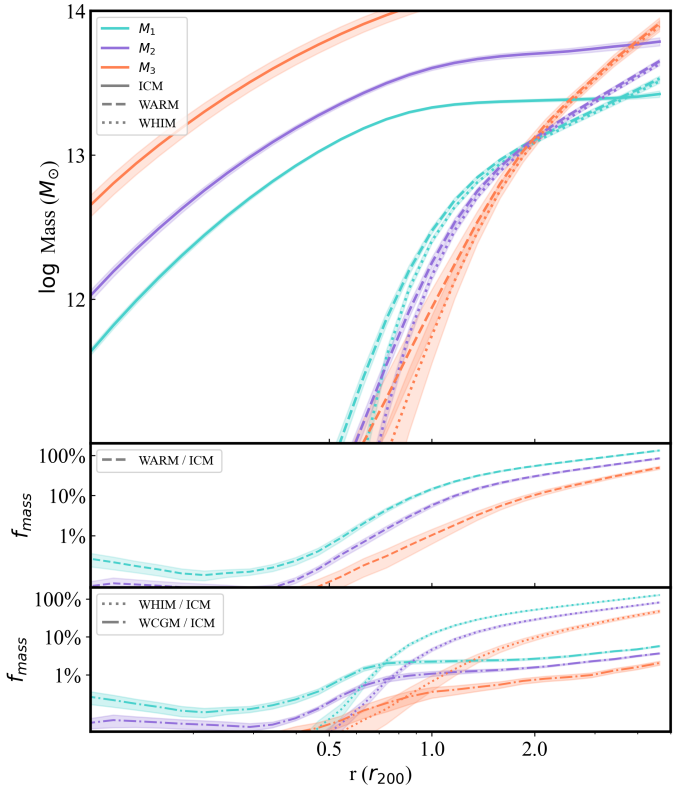

Fig. 2. Top panel: Mean radial profiles of the integrated ICM (solid lines), WARM (dashed lines), and WHIM (dotted lines) gas masses for the three mass bins M_1(salmon lines), M_2 (purple lines), and M_3 (blue lines). Bottom panels: Radial profile of the mass fraction of WARM gas (second panel), composed of WHIM and WCGM (third panel), in the hot ICM mass. The error bars are the error on the mean.

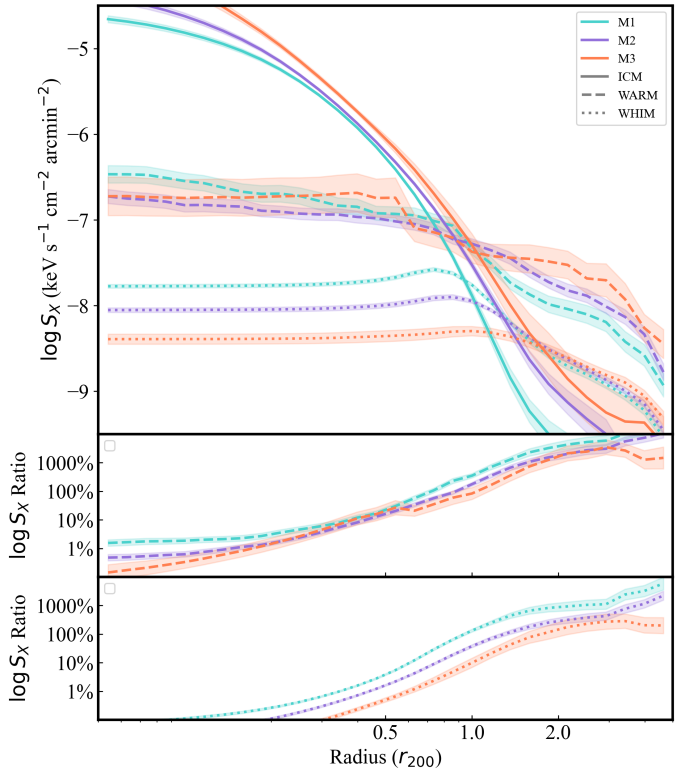

Fig. 3. Top panel: Mean radial X–ray surface brightness profiles for the three cluster mass bins (M_1, M_2, and M_3) simulated in the 0.2–0.4 KeV band. Bottom panels: WARM–to-ICM (dashed lines) and WHIM–to-ICM (dotted lines) surface brightness ratios. The error bars are the error on the mean.

from the different gas phases (ICM, WARM, and WHIM) as a function of the cluster–centric distance. This emission ratio of the HOT and WARM gas must be consistent with the observed soft X-ray excess, which is defined as the excess counts above the expected hot ICM emission. It is compared to recent observations in Sect. 3. The hot ICM dominates the soft X–ray emission up to approximately the virial radius (<1 r_{200}) for all mass ranges, as expected. To highlight the importance of other gas phases for the soft-X-ray emission, the lower panels of Figure 3 plot the WARM–to-ICM and WHIM–to-ICM surface brightness ratios for the three mass samples. Based on these radial profiles, we interpret the main features of the soft X–ray emission from the different gas phases below.

- At all radii and for all mass ranges, the WCGM gas in the WARM phase apparently systematically boosts the soft-X emission because its density is higher. In contrast, the diffuse WHIM gas alone produces less soft-X ray emission per unit mass.
- Within the virial radius ($1 \times r_{200}$), the dominant source of soft X–ray emission is the hot ICM. The second main contribution from the subvirial gas comes from the high–density WCGM, and the diffuse WHIM provides almost no emission up to $0.5 \times r_{200}$. This is true regardless of the cluster mass. By comparing the WARM–to-ICM and WHIM–to-ICM surface brightness ratios, we found that the contribution from WARM gas contribution is far higher inside the clusters than that of the WHIM (<$1 \times r_{200}$). This strong radial evolution of the WARM–to–ICM surface brightness ratio, which reaches 100% at $1 \times r_{200}$, arises from the rapid increase in the WARM gas mass inside the clusters, as illustrated in Fig. 2.
- At the periphery of the cluster and beyond (>$1 \times r_{200}$), the WARM gas predominantly contributes to the soft X–ray surface brightness. Notably, in this radial range, the higher the cluster mass, the more pronounced the emission from the WARM gas. The analysis of the WARM-to-ICM and WHIM-to-ICM surface brightness ratios at these cluster distances reveals that the low-density WHIM gas primarily accounts for the soft X-ray excess, and that the contributions from the high-density WCGM serve as an enhancement. As highlighted in Fig. 2, the WCGM gas mass is considerably lower than that of the WHIM gas at these radii.

3. Comparison between IllustrisTNG predictions and soft X–ray observations

This section compares observations of the soft X–ray emission and our predictions from IllustrisTNG simulation. The X–ray surface brightness has a large cluster–to–cluster scatter beyond the mass dependence. We therefore focus on the relation between relevant gas properties (fraction of the gas phase and location in the subhalos and filaments) and soft X–ray excess in more detail in Sect. 4 after we present the main comparison between simulations and observations in this section.

3.1. Comparison with the soft-X-ray emission profiles

Figure 4 compares the total X–ray surface brightness (i.e., adding contributions from the hot-ICM and the WARM gas)

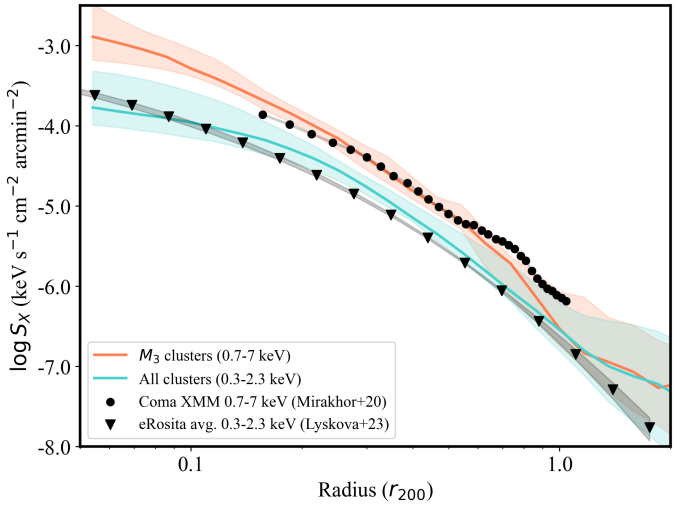

Fig. 4. Median X–ray surface brightness profiles from M_1 and M_3 clusters in the main–band X–ray ranges. The 0.3–2.3 keV range to match the best–fit model of the eRosita observations by Lyskova et al. (2023) is shown in green, and the band of 0.7–7 keV to match the observations of Coma (Mirakhor & Walker 2020) is shown as a blue curve. The error bars in the simulated profiles are the percentiles from 20% to 80%.

for simulated cluster samples in the X–ray band of interest with selected observational results in main–band soft X–rays (0.3−2.3 keV for eRosita, and 0.7−7 keV for XMM Newton). As a first comparison, Figure 4 illustrates the overall reasonable agreement between our analysis of the IllustrisTNG simulation and X–ray observations of the X–ray surface brightness. The soft X-ray emission of the massive Coma cluster measured by Mirakhor & Walker (2020) in the 0.7–7 keV band, illustrated as circles, matches the largest population of massive IllustrisTNG clusters well (mass range M_3; orange curve). Moreover, the averaged surface brightness profile of eRosita clusters measured by Lyskova et al. (2023), as triangles, agrees well with the surface brightness profiles from our full sample of 138 simulated cluster groups. The two comparisons thus indicate that the IllustrisTNG simulation is consistent in general with recent available X–ray observations, although the core slope can be affected when clusters have a cool core (e.g. Arnaud et al. 2002; Braspenning et al. 2024), and the external slope of the profile is probably affected by the environment of the cosmic web, such as gas filaments and clumps, as investigated further below.

3.2. Comparison with observations of the soft X–ray excess

We used the analysis of the soft X–ray excess described in Sect. 2.3 to compare the IllustrisTNG predictions with cluster observations. The soft excess emission is usually reported as a fractional excess of counts in a given annular region above the contribution from the hot ICM. This is equivalent to the ratio of the soft X–ray surface brightness of the HOT and WARM phases shown in Fig. 3.

The left panel of Figure 5 compares the IllustrisTNG predictions with the Bonamente et al. (2002) (hereafter B02) observations of the 0.2–0.4 keV band soft excess in a large sample of ROSAT clusters. The soft excess emission of about 18 of the 38 clusters observed with ROSAT is statistically significant. The mean and standard deviation of the excess in the entire sample is shown as a shaded area in two broad radial bins: $r \leq 0.17$ Mpc with an excess of 2.4 ± 5.7%, and $0.17 \leq r \leq 1$ Mpc with an excess of 13 ± 20%, converted into the approximate r/r_{200} in the figure. The specific data points of the 5 clusters with the largest radial coverage in the sample are also shown individually to highlight the typical detection significance. The typical predicted soft excess in IllustrisTNG in the 0.2–0.4 keV band is at the level of 0.1 to a few dozen percent, which agrees in general with the overall ROSAT observations. Figure 5 also compares the soft excess predictions between the M_3, M_2 and M_1 simulated samples. In particular, the lower–mass samples (M_2 and M_1) predict a relatively higher central soft excess of up to 10%, which may be more consistent with certain observed clusters, such as Abell 2744 and Abell 2255. Our result suggests that the soft excess in the core of our simulated clusters might be slightly lower than in observations on average (for $r \lesssim 0.2\ r_{200}$). This might be explained by the simulation resolution (approximately a few kiloparsec), unresolved clumps, and by the fact that we did not account for nonthermal processes (see the discussion in Sect. 5).

The right panel of Figure 5 compares the Bonamente et al. (2022) (hereafter B22) ROSAT observations of Coma out to the virial radius in the broader 0.2–1 keV band to the corresponding IllustrisTNG predictions. The agreement is very good at all radii, especially near the virial radius, where ROSAT measured a ≥100% soft excess. This agrees with the M_4 sample, which comprises the five more Coma–like massive clusters in IllustrisTNG. It is useful to remark that the B22 results are a combination of the Bonamente et al. (2003) ROSAT fluxes with a reanalysis of the hot ICM that is based on the more recent XMM–Newton observations of Coma by Mirakhor & Walker (2020) in order to refine the hot ICM predictions in the soft band.

3.3. Detectability of the soft-X-ray emission

We complement our analysis of the soft X–ray excess emission in the circumcluster environment by providing an outlook on the detectability of the soft excess according to the IllustrisTNG predictions. The previous section has already shown that the available soft excess measurements are clearly consistent with our predictions. This section provides additional considerations, including the possibility of future detections near the virial radius, which are currently limited to the Bonamente et al. (2003) and Bonamente et al. (2022) ROSAT detections in the Coma cluster.

Figure 6 shows the soft X–ray surface brightness of the HOT, WARM, and ALL gas in the two bands of interest in order to assess whether the detection of the warm subvirial gas near clusters is possible. For comparison, we also show the average surface brightness of the soft X–ray sky as measured by ROSAT (Snowden et al. 1995) as a measure of the typical intrinsic sky background level that is expected to be present at these wavelengths. The error bars in the simulated profiles represent the percentiles from 20% to 80%. We approximated the R12 ROSAT band with the 0.2–0.4 keV band, and we used an average effective area of the ROSAT position–sensitive proportional counter (PSPC) of 120 cm^2 (see, e.g., Fig. 1 of Snowden et al. 1994). The diffuse background at energies near 1/4 keV is highly variable in time and space, and we considered an average background surface brightness of 300–600 × 10^6 counts s^{-1} arcmin^{-2} (in ROSAT units, see Snowden et al. 1997). This figure is representative of the average background at low Galactic latitudes, where the Bonamente et al. (2002) sample was selected, in order to avoid a region with a high Galactic column density that would prevent the observation of soft X–ray fluxes. For the R34 ROSAT band, we used a PSPC effective area of 50 cm^2 and approximated

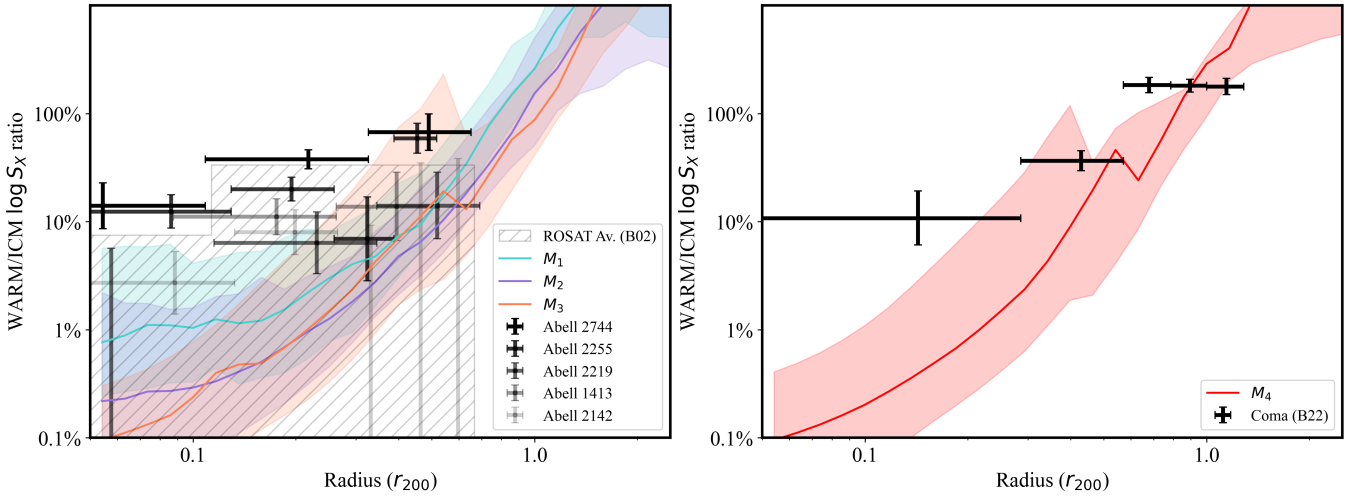

Fig. 5. Left panel: Median WARM–to–ICM surface brightness ratio in the 0.2–0.4 keV band for the three cluster mass bins and the ROSAT results of Bonamente et al. (2002) for a sample of 38 clusters. Right panel: Median WARM–to–ICM surface brightness ratio in the 0.2–1 keV band for clusters in the M_4 mass bins and the observational results of the soft-X-ray excess from the Coma cluster (Bonamente et al. 2022). For each line, the shaded area represents the 20th to 80th percentiles of the soft excess within each cluster sample.

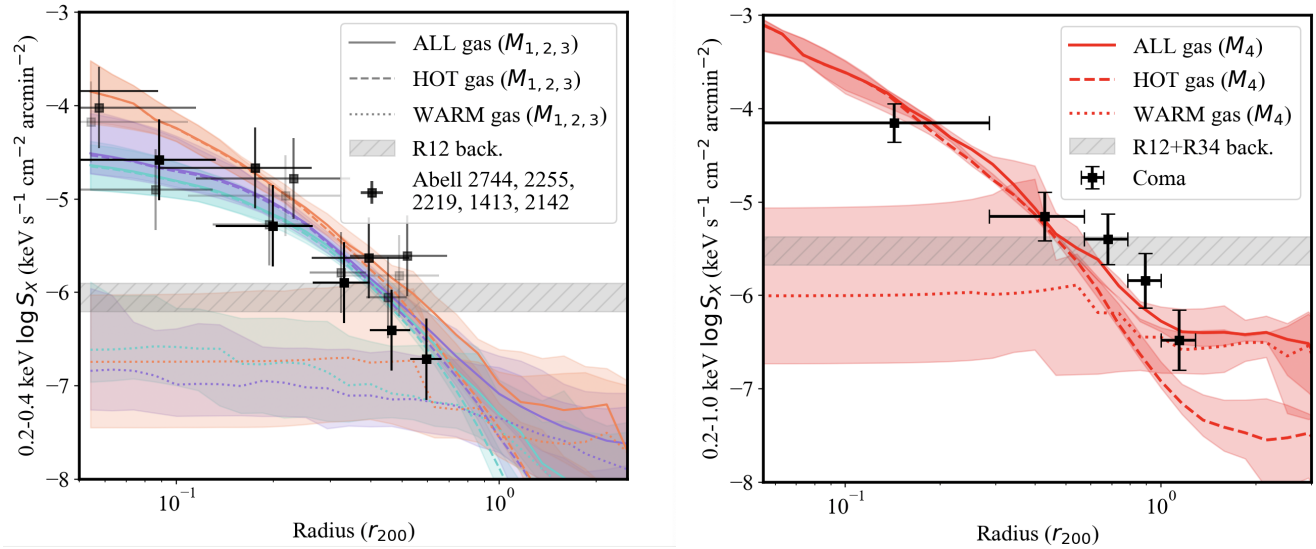

Fig. 6. Left panel: Median soft X–ray surface brightness of the WARM and ICM phases and the ALL gas in the 0.2–0.4 keV band, approximately equivalent to the ROSAT R12 band of the B02 data. Right panel: Median soft X–ray surface brightness in the 0.2–1 keV band, corresponding to the B22 data. For each line, the shaded area represents the 20th to 80th percentiles within each cluster sample. The R12 band corresponds to approximately 0.2−0.4 keV, and the R34 band corresponds to ∼0.4−1.0 keV (Snowden et al. 1995, 1997).

it with the 0.5–1 keV band, and we considered a typical diffuse background of 100–200 × 10^6 counts s^{-1} arcmin^{-2}. The R34 band soft-X–ray sky is considerably less variable than in the R12 band, and this background level is generally representative of most sight lines (see Fig. 6).

The surface brightness of the WARM gas, especially in the 1/4 keV band, can be substantially lower than the typical diffuse background. For the more massive cluster (M4, right panel), the WARM gas surface brightness is comparable to the background in the inner cluster regions. Near the virial radius, the WARM gas is lower by at least a factor of 10 than the sky background. This means that accurate soft excess fluxes can only be measured using a careful estimate of the background, preferably using contemporaneous and in situ background measurements, as was the case for the Bonamente et al. (2002) and Bonamente et al. (2022) observations. Moreover, the ∼0.5−1 keV diffuse background is lower and more stable than in the 0.2−0.4 keV band, as shown by the ROSAT All–Sky Survey maps of Snowden et al. (1997), for instance, and it is therefore more suitable for cases when local background is not available.

For the detection of the soft excess in the inner regions, the main advantage is provided by the inherently higher surface brightness of the WCGM, which is the dominant soft excess–producing phase (Fig. 6). The soft excess in the inner regions is therefore less affected by the background subtraction (see, e.g., Bonamente et al. 2002; Nevalainen et al. 2007). Challenges for the detection in the inner regions are associated with the accurate determination (and therefore, removal) of the ICM gas because the soft excess is only expected to be a few percent above the surface brightness of the hot ICM (Fig. 3). In the inner cluster regions, the ICM temperature and abundance structure can be complex (e.g. Rasia et al. 2014; Mernier et al. 2017), including

for the presence of cool cores. This leads to systematic uncertainties in the detection of soft fluxes from warm subvirial gas.

Near the virial radius, the surface brightness of the soft excess becomes comparable to that in the hot ICM, and therefore, the details of the hot ICM are less important for the detection of the soft excess. At these radii, the main challenge is an accurate background subtraction because the soft excess is typically lower than the diffuse soft X–ray background. The ideal means for the detection of the soft excess near and beyond the virial radius are large–scale surveys such as the ROSAT All–Sky Survey (RASS, Voges et al. 1999) or the eRosita survey (e.g. Liu et al. 2022) because of their contemporaneous and in situ background measurements. The analysis by Bonamente et al. (2009) of the RASS data near Coma confirmed the detection of the soft excess from pointed observations (Bonamente et al. 2003), and they tentatively extended the detection of the soft excess halo out to $\sim 2-3 \times r_{200}$. The soft excess emission is therefore detectable in the inner cluster regions and near the virial radius. This is consistent with available observations.

To date, no measurements of the soft excess are available in the region beyond the virial radius. As a proof of concept of the detectability of the soft excess in the $1-2 \times r_{200}$ region, we considered the 0.2-1 keV band (right panel of Fig. 6). In this region, the WARM surface brightness depends on the mass of the host cluster, and it is approximately $\log S_X \sim -6.5$. The emission of the most massive Coma–like clusters is higher, and we therefore assumed $\log S_x = -6.5$ as a reference value for a background of $\log S_{x,b} = -5.5$ (combination of the R12 and R34 band backgrounds), that is, the WARM signal is 10% of the average background level. For clusters at $z = 0.1$ and with $r_{200} = 1.5$ Mpc, it is immediately clear that a 100 ks observation with the ROSAT PSPC in the 0.2–1 keV band yields $7.3 \pm 0.1 \times 10^3$ source counts against a background of $73 \pm 0.3 \times 10^3$ counts. When other sources with systematic errors associated with the background subtraction can be controlled, this exposure time is more than adequate to deliver a detection of the WHIM in emission from the circumcluster environments. Similar considerations can be applied to the eRosita survey, for example, but with a somewhat higher background[1].

These IllustrisTNG data should not be extrapolated much beyond the virial radius in order to predict the expected count rates of the WARM and WHIM gas. The data we considered to make the radial profiles only include particles within $5 \times r_{200}$, and no outer layers of the gas were included in the calculation of the projected surface brightness profiles (see Paper I, Gouin et al. 2023). Beyond the virial radius, the WHIM gas becomes preferentially distributed in filamentary structures, as shown by Galárraga-Espinosa et al. (2020, 2021), Tuominen et al. (2021). Therefore, it becomes more meaningful to seek the detection of this warm gas in specific filament regions and not in azimuthally averaged annuli, as we did here.

4. Possible origins of the soft X–rays excess

In Sect. 2 we computed the thermodynamic property profile of TNG clusters (see Fig. 1) to predict the cluster X-ray emission and the soft-X-ray excess by separating the HOT and WARM gas phase (see Fig. 3). These predictions match recent and previous observations from ROSAT, XMM, and eRosita well, as shown in Sect. 3 (see Figs. 4 and 5). As suggested by Gouin et al. (2023), the clumpy WCGM gas is required in addition to the diffuse WHIM gas to explain the soft excess in observations. In this section, we aim to understand the origin of the soft X–ray excess better as a function of the cluster distance.

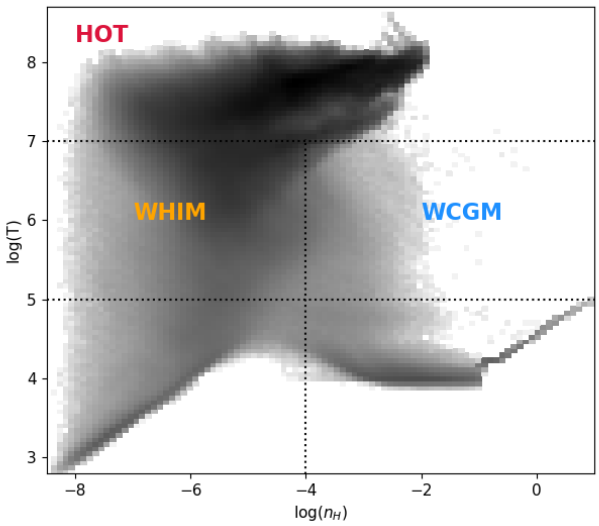

Fig. 7. Temperature-density diagram for all gas cells around a representative IllustrisTNG cluster up to 5 r_{200}, with the three gas phases of interest, HOT, WHIM, and WCGM.

4.1. Visualizing WCGM and WHIM gas

To understand the origin of the soft X–ray emission better, we illustrate in Fig. 7 and Fig. 8 the three main gas phases (HOT, WCGM, and WHIM gas) and their distribution around a simulated cluster. As expected, the clumps of WARM gas are in the form of WCGM gas because this phase is by definition high-density warm gas. The other phase that contributes to the WARM gas, the WHIM (rightmost panel) shows a rather smooth spatial distribution. Interestingly, this WCGM gas apparently strongly populates the subhalos of galaxies inside and around clusters, as illustrated by the green circles, which show galaxies with a stellar mass $M_* > 10^9\, M_\odot/h$. The radius of the green circles is equal to twice the radius containing half of the total mass of each galaxy. These galaxies correlate very well with the spatial distribution of WCGM gas, as expected from the lower-density threshold that defines this gas phase Martizzi et al. (2019). In agreement with Angelinelli et al. (2021), the gas clumps tend to trace filamentary patterns around clusters. The cosmic web skeleton, shown as black lines, was computed by using the algorithm called TREX filament finder (Bonnaire et al. 2020) on 3D galaxy distribution, similarly to Gouin et al. (2022). The right panel of Fig. 7 qualitatively confirms that the WHIM gas traces the filaments that are connected to clusters.

4.2. Definition and computation of the gas fraction

The gas-phase fraction

To explore the effect of the gas-phase abundance on the soft X–ray excess, we computed its mass fraction as

$$f_i(r) = \frac{M_i(r)}{M_{\text{all gas}}(r)}\,, \tag{3}$$

[1] It goes beyond the scope of this paper to provide a feasibility of WHIM detection with X–ray missions. However, ROSAT has a ≥99% particle background rejection (Plucinsky et al. 1993), which makes it uniquely suited for soft X–ray detections.

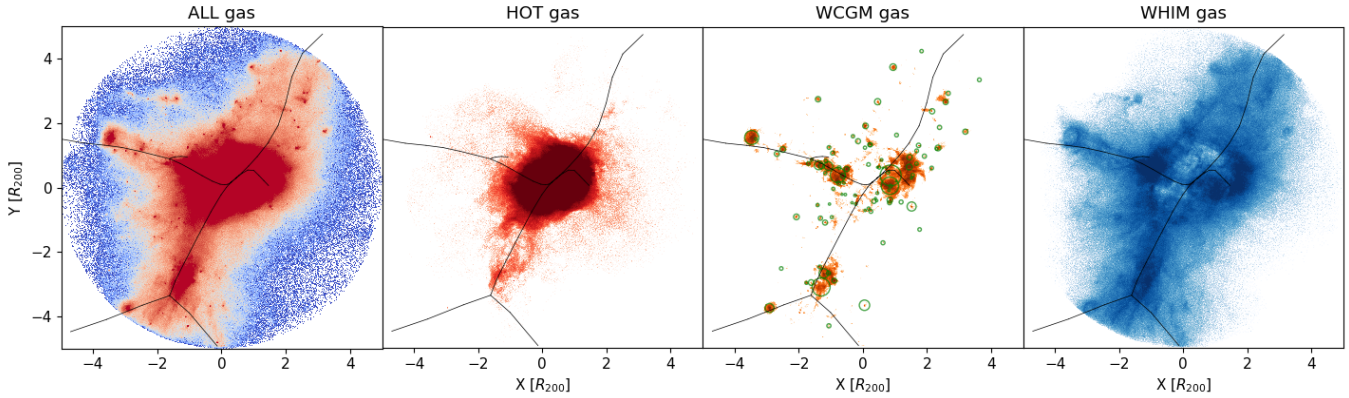

Fig. 8. Gas distribution as a function of the different phases as defined in Table 1 around a representative IllustrisTNG cluster. We overplot the cosmic filaments detected by T-REX algorithm as dark lines. We overplot the galaxies (with a stellar mass $M_* > 10^9\ M_\odot/h$) as green circles with radii proportional to the galaxy mass.

with i the gas phase (WCGM or WHIM), and r the clustercentric radius enclosing the total gas mass ($M_{\text{all gas}}$) and the mass of the ith gas-phase (M_i). We chose a radial range from $R = 0$ to 5 r_{200} in intervals of $1 \times\ r_{200}$ to accurately probe the radial evolution.

The gas fraction in filaments

To explore whether the soft X–ray emission is the result of either WCGM gas surrounding galaxies and/or WHIM gas inside filaments, we selected the gas inside filaments and/or inside subhalos. We considered gas located in filaments to be gas cells enclosed within 2 Mpc/h around the filament spine (which is a conservative value for the typical radial thickness of filaments based on their density profiles Galárraga-Espinosa et al. 2020; Wang et al. 2024). We excluded gas cells from galaxies, which are defined as those inside twice the half-mass radius of each galaxy with a stellar mass $M_* > 10^9\ M_\odot/h$. The cosmic filaments were detected with the T-REX algorithm in galaxies with a stellar mass $M_* > 10^9\ M_\odot/h$ inside spheres with a radius of $10 \times r_{200}$ centered on each cluster (similar to Gouin et al. 2021).

We quantified the gas in filaments via

$$f_{\text{gas}}^{\text{fil}}(r) = \frac{M_{\text{all gas}}^{\in\text{filaments}}(r)}{M_{\text{all gas}}(r)}\,. \tag{4}$$

For each cluster, we removed the contribution of gas that was included in galaxies that were located in filaments to investigate the effect of galaxies and filaments on the soft X–ray excess separately.

The gas fraction in substructures

Similarly, we computed the fraction of gas that surrounded massive galaxies ($M_* > 10^9\ M_\odot/h$) as

$$f_{\text{gas}}^{\text{gal}}(r) = \frac{M_{\text{all gas}}^{\in\text{galaxies}}}{M_{\text{all gas}}}\,. \tag{5}$$

For each cluster, we did not consider the main central galaxy to exclude the contribution of the cluster itself. Again, we considered the gas cells in galaxies to be the gas inside twice the half-mass radius of each galaxy.

The subhalo mass fraction

Finally, the subhalo mass fraction was estimated from

$$f_{\text{sub}}(r) = \frac{\sum_{\text{sub}\in\text{r}} M_{\text{sub}}}{M_{\text{main}}}\,, \tag{6}$$

where M_{sub} is the total mass of a given subhalo inside the radial annulus r, and M_{main} is the total mass of the main subhalo for each cluster. Only for the computation of f_{sub} did we consider all the subhalos extracted by the *Subfind* algorithm (without any mass selection) to fully capture the mass contained in clumps. It therefore reflects the relative clumpiness of the matter distribution.

4.3. Correlation of the soft X–ray excess with the gas properties

For each cluster, we integrated the soft X–ray excess, which is defined as the ratio of the WARM to the HOT gas X–ray emission and is hereafter referred to as $\log S_X^{\text{ratio}}$, inside different radial annuli centered on the clusters with radial ranges of [0−1], [1−2], [2−3], [3−4], and [4−5] r_{200}. We analyzed the correlation between the integrated soft X–ray excess and the gas properties by computing the Spearman correlation coefficient and its associated p value. The integrated soft X–ray excess presented Fig 9 and Fig 10 wa calculated for the energy band 0.2–1.0 keV.

In Fig. 9 we show the correlations between the soft X–ray excess and the gas properties as a function of cluster distance. We observe a smooth radial evolution in the soft excess influences, with a gradual transition. As detailed in Fig. 10, this can be divided into three radial regimes: inside clusters at $r < r_{200}$ (top panel), near the virial radius at $1 < r/r_{200} < 2$ (middle panel), and outside clusters at $r > 2 \times r_{200}$ (bottom panel). The soft X–ray excess in the two figures is anticorrelated with the cluster mass in all radial ranges. As anticipated from Fig. 3, clusters with a lower mass exhibit a greater soft excess. Except for the cluster mass, all correlations are therefore the partial correlation coefficient, which is defined as the degree of association between the soft excess and the gas properties after the effect of the primary variable is removed, that is, the dependence on mass. Beyond this mass-driven effect, we interpret the correlations between the soft X–ray excess and gas properties as listed below.

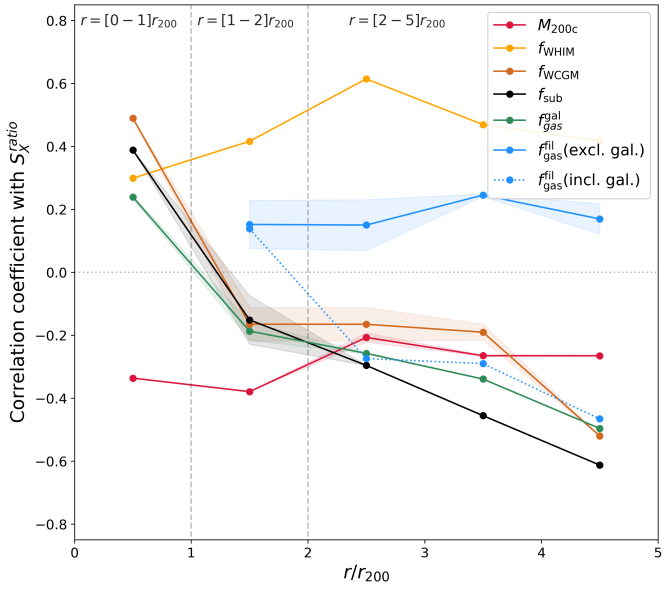

Fig. 9. Radial evolution of the Spearman correlation coefficient between the soft X–ray excess ($S_X^{\rm ratio}$) and gas properties as a function of cluster distance R. The p values are represented by the error bars. We present the direct correlation with cluster masses (red line), but the other properties were computed by using the partial correlation to first remove any mass dependence.

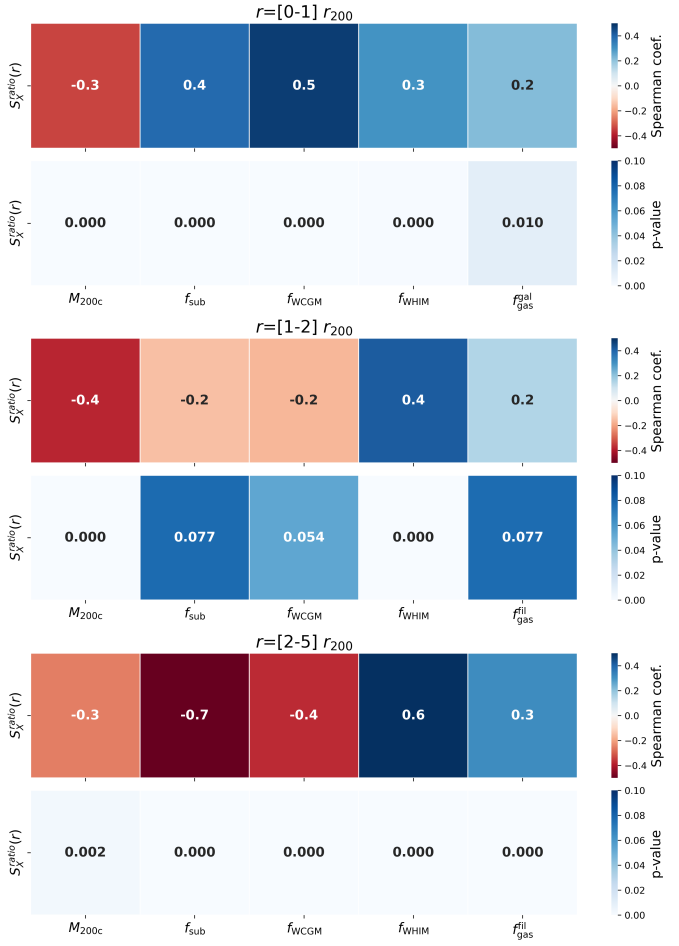

Fig. 10. Spearman correlation coefficient between the soft excess and the cluster gas properties and its associated p values, integrated over three radial ranges: inside clusters $0 > R[r_{200}] > 1$, around clusters $1 > R[r_{200}] > 2$, and outside clusters $2 > R[r_{200}] > 5$. As in Fig 9, except for the cluster mass (M_{200}), we show the partial Spearman correlation to remove any mass dependence.

(i) Inside clusters ($r < r_{200}$), the soft X–ray excess correlates strongly with the WCGM gas fraction, the fraction of substructures, and the fraction of gas inside satellite galaxies. This suggests that the soft X–ray excess is mainly produced by substructures that host WCGM gas (with a correlation factor of 0.5 in the top panel of Fig. 10). The WHIM gas inside clusters also affects the soft X–ray excess, but with a lower correlation factor of 0.3. Marini et al. (2025) recently discovered that luminous soft X–ray galaxy groups are more recently formed than their fainter counterparts with similar masses. Consequently, we speculate that the soft excess inside clusters, which correlates with the substructure fraction, is a proxy for a different dynamical state that is induced by a different mass-assembly history. We recall that Marini et al. (2025) explored the soft X-ray luminosity, and not specifically the soft X-ray excess.

(ii) Around clusters ($1 < r/r_{200} < 2$), the role of the WHIM gas becomes more significant, with a correlation factor of 0.4. The correlation with other properties has high p values, however, which makes it difficult to distinguish the effect of WCGM gas clumps and WHIM filaments on the soft excess in this particular regions, as shown in the middle panel of Fig. 10. The reason might be that these cluster boundaries are transitioning regions, in which WARM gas is in-falling, out-flowing, and shocking during the accretion process (Rost et al. 2021).

(iii) Outside clusters ($2 < r/r_{200} < 5$), the soft excess is mostly induced by WHIM gas inside cosmic filaments. We found that the soft X–ray excess tends to correlate with the fraction of gas in filaments (only when the gas in galaxies is excluded), and it correlates strongly with the WHIM fraction (blue and yellow points in Fig. 9). The strong anticorrelation with the WCGM and other substructure fractions also suggests that the more diffuse the gas, the higher the soft X–ray excess in this region.

To further test whether the soft excess results from a substructure inside the clusters and from the diffuse WHIM outside, we performed the following two selections. First, we defined less clumpy systems as those in the lowest 25% of the substructure fraction and WCGM fraction inside r_{200}, indicating spatially clumpy clusters. We obtained a selection of 14 clusters. Conversely, the more clumpy systems were selected as those in the highest 25% of both parameters, representing clumpy clusters with a larger fraction of dense clumps. This resulted in a selection of 15 clusters. The left panel of Fig. 11 confirms our finding that the soft X-ray excess in unrelaxed clusters is significantly higher inside 0.5 r_{200} than in relaxed objects. Second, we considered systems that are strongly populated by the diffuse WHIM outside the virial radius (between 1 and 5 $\times r_{200}$) as those in the lowest 25% of the substructure fraction and the highest 25% of the WHIM fraction. This resulted a selection of 21 clusters with a more diffuse WHIM. Conversely, systems with a less diffuse WHIM in their outskirts were selected as those in the highest 25% of the substructure fraction and the lowest 25% of the WHIM fraction outside the virial radius, representing less diffuse and more clumpy cluster environments. This resulted a selection of 12 clusters. The right panel of Fig. 11 confirms that the soft excess in cluster outskirts that are strongly populated by

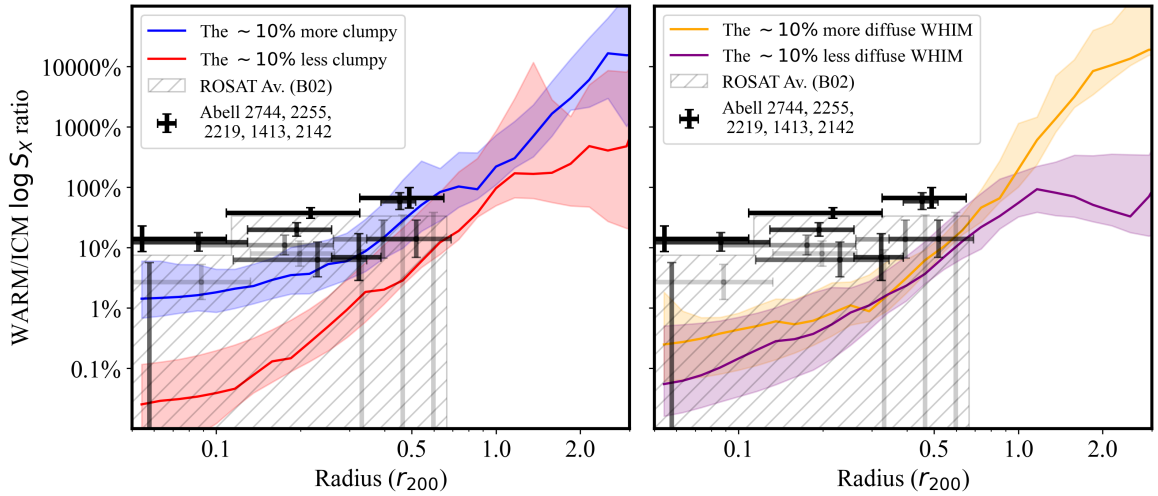

Fig. 11. Median soft excess of four cluster populations with different gas-phase and substructure fractions (details in Sect. 4.3). The error bars represents the percentiles from 20% to 80%.

WHIM gas is significantly higher at radii $>1\times r_{200}$ than for those with clumpy environments.

5. Discussion

5.1. Interpretations of the soft excess inside clusters

The soft excess detected inside clusters can be explained by the thermal emission of subvirial WARM gas. Inside the virial radius, the WARM gas is substantially more clumpy that the hot ICM (see Fig. 1), with a significant mass fraction (from 0.1% to more than 10%; see Fig. 2) producing the inner soft excess at a level of 0.1 to more than 10% of the hot ICM emission (see Fig. 3). Its large scatter is consistent with the detection of only ∼40% of clusters with a soft excess with ROSAT (see Fig. 5).

Exploring the origin of the inner soft X–ray excess, we found that the large observed scatter might be explained be the large variety of dynamical cluster states (see Fig. 11). We found that the soft excess is stronger for the more clumpy clusters. This trend is significant, and the excess decreases from 1–10% for the more clumpy objects to less than 0.1% for the most homogeneous ones (see Fig. 11). Our results suggests that the soft X–ray excess is mainly produced by substructures that host WCGM gas (see Fig. 7). This interpretation of a soft X–ray boost inside clusters also agrees with previous studies that found that inhomogeneities boost the estimates of the X-ray emissivity (see e.g. Planelles et al. 2017; Ghirardini et al. 2018).

Systems that experienced a recent merger (i.e., that are still below the virialization timescale) are expected to be more clumpy, with residual BCGs and satellites originating from the two merging halos. These substructures are expected to be surrounded by WARM gas in the form of WCGM (as illustrated in Fig. 8). In these recently formed systems, the ICM is expected to be not yet fully virialized, but rather in multiphase and inhomogeneous. A contrast might therefore occur between the hard X-ray emission from the virialized hot ICM and the soft emission produced by the inhomogeneous WARM gas that is still being mixed and incorporated into the hot component. Recently, Marini et al. (2024) found that X-ray bright objects in their cores (i.e., within r_{500}) exhibit rapid mass accretion during the later stages of their evolution in the Magneticum simulation (Dolag et al. 2016). Additionally, Gouin et al. (2022) demonstrated a strong correlation between the formation time, accretion rate, and degree of relaxation of a cluster with the asymmetries in its gas distribution. Based on these studies, we infer that a high excess of soft X-rays is related to an unrelaxed cluster as a consequence of a late-stage mass-assembly history. In contrast, relaxed clusters that formed early are expected to preferentially have a lower soft excess.

Even though we tended to reproduce most of the soft excess in the central regions as thermal emission from warm gas clumps, we remain limited by the resolution of the simulation (∼ kiloparsec). In addition to the contribution from unresolved clumps, we also did not account here for nonthermal processes, such as turbulence and shocks, that are injected into the ICM (Vallés-Pérez et al. 2021; Lebeau et al. 2025).

5.2. Interpretations of the soft excess around clusters

Near the virial radius, the WARM gas density dominates the hot ICM. The exact value of this transition from ICM to WARM depends on the cluster mass (see Fig. 2) in such a way that massive clusters have an ICM phase that is more spatially extended than low–mass clusters. This finding suggests that the soft excess might preferentially occur at larger radii in more massive clusters, as was indeed observed in the case of Coma (see Fig. 5, Bonamente et al. 2003). The Coma cluster is the only case to date for which a strong soft excess emission was detected up to the virial radius. The study by Bonamente et al. (2002) of a large sample of ROSAT clusters did not attempt to measure the soft excess beyond this radius, where the data were dominated by background (see Fig. 6), and therefore, there is no statistically significant cluster sample so far for which these predictions have been tested. Our predictions of the soft X–ray excess reproduce the Coma observations near the virial radius very well by considering WCGM clumps and diffuse WHIM gas. This result is consistent with the finding by Churazov et al. (2023b) that the Coma soft excess cannot be reproduced by assuming WHIM gas alone.

Further insights into the origin of the soft X-ray excess in this region remain challenging, as evidenced by the fact that only the WHIM fraction shows a strong correlation with the excess (see Fig. 10). This is due to complicated physical processes in the cluster peripheries that are induced by diffuse material that collapses toward filaments and gas-shock processes triggered by substructures. Rost et al. (2021) have studied the complex

velocity field of gas in this regions in detail and showed that gas preferentially enters the cluster as part of a filament and leaves the cluster outside filaments (see also Rost et al. 2024). Additionally, the main gas-accretion shock in the clusters is expected in this radial regions, for instance, near $1.5 \times r_{200}$, according to Arthur et al. (2019). Similarly, Vurm et al. (2023) have also found the formation of a gas shock where filaments were connected the hot atmosphere of clusters in the C-EAGLE simulation. Power et al. (2020) demonstrated that baryonic physics models of simulations converge on the time and location of shocks, but differ in the shock strength. Moreover, Lebeau et al. (2024) discussed the distinction between gas and the dark matter splashback radius and argued that the detection of the splashback radius in pressure profiles might be more related to an accretion shock. In this line, Churazov et al. (2023a) have studied the complex geometry of the accretion shock in this region around the Coma cluster. This transition from HOT-to-WARM gas contains a complex mixture of infalling and outflowing gas, including potential backsplash gas (Gouin et al. 2022; Kotecha et al. 2022). This complicates the study of this peripheral region.

5.3. Interpretations of the soft excess outside clusters

It is important to point out that the meaning of the soft X–ray excess outside clusters ($> 2\ r_{200}$) is different from its usual definition as an excess of soft-X emission above the hot ICM inside a given cluster. In this circumcluster medium, the excess now refers to the relative importance between soft X–ray emission from warm and that of hot gas induced by any structures that are neighbor to the central cluster, and not just the central cluster itself. An investigation of this region will be the subject of a follow–up paper, which will focus on the X-rays emission by distinguishing the structures (clusters, groups, filaments, and clumps) instead of the current X-ray ratio of the gas phases. This study goes beyond the scopes of this paper.

In general, we predict that clusters of all masses feature a total WARM mass of $\sim 2 \times 10^{13}$ $M_\odot$ within $2 \times r_{200}$, which corresponds to approximately 10% of the ICM mass for the more massive clusters and to ∼50% for the low-mass clusters (see Fig. 2). We showed that at $5 \times r_{200}$, the WARM halo mass is comparable to that of the hot ICM, in particular, for the cluster mass range M_1 and M_2 with $\log M < 14.5$. This indicates that the circumcluster warm gas is a significant reservoir of baryons, of which the soft excess emission near the virial radius represents only a very small part. This outer region from 2 to 5 r_{200} is dominated by WHIM gas that is mostly located inside cosmic filaments (Galárraga-Espinosa et al. 2021; Tuominen et al. 2021). At this scale, our findings indicate that the soft excess is correlated with the WHIM fraction and gas abundance in filaments (see Fig. 10). This shows that lower fraction of substructures leads to a higher soft excess (see Fig. 11).

5.4. Detectability of warm gas in cluster peripheries

Only a few detections of individual WHIM filaments in emission were made so far, starting from filaments toward superclusters (Kull & Böhringer 1999; Zappacosta et al. 2005), so-called spider legs around Abell 2744 (Eckert et al. 2015; Gallo et al. 2024), to WHIM bridges between cluster pairs (Sakelliou & Ponman 2004; Werner et al. 2008). More recently, the detection of a soft-X–ray filament between Abell 3391 and Abell 3395 with eRosita was reported by Reiprich et al. (2021) and was also studied by Alvarez et al. (2018), and a filament between Abell 2029 and Abell 2033 was also reported (Mirakhor et al. 2022) that was previously identified from ROSAT (Walker et al. 2012). Recently, Dietl et al. (2024) identified an X-ray excess beyond thrice the virial radius of Abell 3667, which is indicative of an intercluster filament. Recent research focused on stacking intercluster gas filaments to enhance the signal-to-noise ratio for detecting warm gas (Tanimura et al. 2022; Zhang et al. 2024b). Another possibility is the detection of the WARM gas via their emission lines. Zhang et al. (2024a) recently used the 30 most massive and relaxed IllustrisTNG clusters to show that they enable the use of emission lines for measuring the thermodynamic, chemical, and kinematic properties of the gas up to r_{200} and beyond with future missions, in particular, with the Line Emission Mapper (LEM) (see also Tuominen et al. 2023). For further exploration, Zhao et al. (2025) recently provided forecasts for WHIM detections outside clusters with the proposed mission called Hot Universe Baryon Surveyor. Our results indicate that the soft X–ray emission from WARM gas in the cluster environment might be detectable toward the region immediately outside of the virial radius, as shown in Sect. 3.3. At these radii, the gas is mostly in the form of diffuse WHIM filaments, which are known to have a higher density toward galaxy clusters (Li et al. 2025). We argue that the region outside of the virial radius of massive clusters is ideal for detecting WHIM filaments in emission. The recent detection of soft X–ray emission near clusters (e.g. Reiprich et al. 2021; Mirakhor et al. 2022; Dietl et al. 2024) supports this scenario and indicates that the circumcluster environment is the region in which we should search for X–ray emission of filaments.

6. Conclusions

We investigated the origin of the soft X–ray emission in and near IllustrisTNG galaxy clusters. In general, our results suggest that the WARM gas phase causes an excess of soft X–ray emission above the contribution from the virialized HOT phase, as was observed by a variety of X–ray missions (e.g., Lieu et al. 1996b,a; Bonamente et al. 2002, 2003). In detail, we distinguished three different radial regimes with different gas structures and properties that cause this soft excess. In the inner cluster regions, this soft excess is primarily expected to be due to the high–density and high–clumpiness WCGM phase. Toward the virial radius, the soft excess is given by a combination of two distinct WARM gas phases, that is, the high–density WCGM gas and the low–density WHIM gas. The soft X–ray predictions for the most massive clusters match the observations of the Coma cluster very well, which is the only cluster to date for which soft excess emission to the virial radius was reported (Bonamente et al. 2003, 2009, 2022). Beyond the virial radius, the diffuse WHIM phase becomes the dominant driver of the soft excess in cluster environments. This is consistent with the established picture of galaxy clusters being the nodes at which WHIM filaments converge (e.g. Cen 1998; Davé et al. 2001). The soft X–ray emission from WHIM filaments that project toward the region immediately outside the virial cluster radius (i.e., within a few $\times r_{200}$) is a promising avenue for the detection of WHIM filaments in emission. This radial picture is the natural way to interpret the soft excess as due to WCGM in the inner regions, a combination of WCGM and WHIM near the virial radius (e.g., as in Coma Bonamente et al. 2022), and WHIM beyond the virial radius (Reiprich et al. 2021; Mirakhor et al. 2022; Dietl et al. 2024). Our analysis offers additional clues about the physical conditions that favor soft excess. In particular, clusters with a larger substructure fraction are expected to have a higher central soft excess, and clusters surrounded by

a larger fraction of diffuse WHIM naturally show a high excess beyond the virial radius. While additional details remain to be investigated, these findings provide a relatively simple first–order picture of the origin of the soft X–ray excess in circumcluster environments.

Acknowledgements. The authors thank an anonymous referee for their useful comments and suggestions. CG acknowledge funding from the French Agence Nationale de la Recherche for the project WEAVEQSO-JPAS (ANR-22-CE31-0026). We thank the IllustrisTNG collaboration for providing free access to the data used in this work. This work was supported in part by NASA's Astrophysics Data Analysis Program (ADAP) grant 'Closing the Gap on the Missing Baryons at Low Redshift with multiwavelength observations of the Warm–Hot Intergalactic Medium' awarded to the University of Alabama in Huntsville.

References

Allen, S. W., Schmidt, R. W., Ebeling, H., Fabian, A. C., & van Speybroeck, L. 2004, MNRAS, 353, 457
Alvarez, G. E., Randall, S. W., Bourdin, H., Jones, C., & Holley-Bockelmann, K. 2018, ApJ, 858, 44
Angelinelli, M., Ettori, S., Vazza, F., & Jones, T. W. 2021, A&A, 653, A171
Arnaud, M., Aghanim, N., & Neumann, D. M. 2002, A&A, 389, 1
Arthur, J., Pearce, F. R., Gray, M. E., et al. 2019, MNRAS, 484, 3968
Bahar, Y. E., Bulbul, E., Ghirardini, V., et al. 2024, A&A, 691, A188
Barnes, D. J., Kay, S. T., Bahé, Y. M., et al. 2017, MNRAS, 471, 1088
Bonamente, M., & Nevalainen, J. 2011, ApJ, 738, 149
Bonamente, M., Lieu, R., & Mittaz, J. P. D. 2001a, ApJ, 561, L63
Bonamente, M., Lieu, R., & Mittaz, J. P. D. 2001b, ApJ, 547, L7
Bonamente, M., Lieu, R., Nevalainen, J., & Kaastra, J. S. 2001c, ApJ, 552, L7
Bonamente, M., Lieu, R., Joy, M. K., & Nevalainen, J. H. 2002, ApJ, 576, 688
Bonamente, M., Joy, M. K., & Lieu, R. 2003, ApJ, 585, 722
Bonamente, M., Lieu, R., Mittaz, J. P. D., Kaastra, J. S., & Nevalainen, J. 2005, ApJ, 629, 192
Bonamente, M., Lieu, R., & Bulbul, E. 2009, ApJ, 696, 1886
Bonamente, M., Mirakhor, M., Lieu, R., & Walker, S. 2022, MNRAS, 514, 416
Bonnaire, T., Aghanim, N., Decelle, A., & Douspis, M. 2020, A&A, 637, A18
Bowyer, S., Lampton, M., & Lieu, R. 1996, Science, 274, 1338
Bowyer, S., Berghöfer, T. W., & Korpela, E. J. 1999, ApJ, 526, 592
Braspenning, J., Schaye, J., Schaller, M., et al. 2024, MNRAS, 533, 2656
Cen, R. 1998, ApJ, 498, L99
Cheng, L.-M., Borgani, S., Tozzi, P., et al. 2005, A&A, 431, 405
Churazov, E., Khabibullin, I., Bykov, A. M., Lyskova, N., & Sunyaev, R. 2023a, A&A, 670, A156
Churazov, E., Khabibullin, I. I., Dolag, K., Lyskova, N., & Sunyaev, R. A. 2023b, MNRAS, 523, 1209
Davé, R., Cen, R., Ostriker, J. P., et al. 2001, ApJ, 552, 473
Dickey, J. M., & Lockman, F. J. 1990, ARA&A, 28, 215
Dietl, J., Pacaud, F., Reiprich, T. H., et al. 2024, A&A, 691, A286
Dolag, K., Komatsu, E., & Sunyaev, R. 2016, MNRAS, 463, 1797
Eckert, D., Jauzac, M., Shan, H., et al. 2015, Nature, 528, 105
Finoguenov, A., Briel, U. G., & Henry, J. P. 2003, A&A, 410, 777
Galárraga-Espinosa, D., Aghanim, N., Langer, M., Gouin, C., & Malavasi, N. 2020, A&A, 641, A173
Galárraga-Espinosa, D., Aghanim, N., Langer, M., & Tanimura, H. 2021, A&A, 649, A117
Gallo, S., Aghanim, N., Gouin, C., et al. 2024, A&A, 692, A200
Ghirardini, V., Ettori, S., Eckert, D., et al. 2018, A&A, 614, A7
Gouin, C., Bonnaire, T., & Aghanim, N. 2021, A&A, 651, A56
Gouin, C., Gallo, S., & Aghanim, N. 2022, A&A, 664, A198
Gouin, C., Bonamente, M., Galárraga-Espinosa, D., Walker, S., & Mirakhor, M. 2023, A&A, 680, A94
Hahn, O., Angulo, R. E., & Abel, T. 2015, MNRAS, 454, 3920
Hahn, O., Martizzi, D., Wu, H.-Y., et al. 2017, MNRAS, 470, 166
HI4PI Collaboration (Ben Bekhti, N., et al.) 2016, A&A, 594, A116
Kaastra, J. S., Lieu, R., Tamura, T., Paerels, F. B. S., & den Herder, J. W. 2003, A&A, 397, 445
Kalberla, P. M. W., Burton, W. B., Hartmann, D., et al. 2005, A&A, 440, 775
Kotecha, S., Welker, C., Zhou, Z., et al. 2022, MNRAS, 512, 926
Kull, A., & Böhringer, H. 1999, A&A, 341, 23
Landry, D., Bonamente, M., Giles, P., et al. 2013, MNRAS, 433, 2790
Lebeau, T., Ettori, S., Aghanim, N., & Sorce, J. G. 2024, A&A, 689, A19
Lebeau, T., Zaroubi, S., Aghanim, N., Sorce, J. G., & Langer, M. 2025, A&A, 704, A14
Leccardi, A., & Molendi, S. 2008, A&A, 486, 359
Li, R., Cui, W., Liu, A., et al. 2025, A&A, 701, A37
Lieu, R., Mittaz, J. P. D., Bowyer, S., et al. 1996a, Science, 274, 1335
Lieu, R., Mittaz, J. P. D., Bowyer, S., et al. 1996b, ApJ, 458, L5
Liu, A., Bulbul, E., Ghirardini, V., et al. 2022, A&A, 661, A2
Lyskova, N., Churazov, E., Khabibullin, I. I., et al. 2023, MNRAS, 525, 898
Mantz, A. B., Morris, R. G., Allen, S. W., et al. 2022, MNRAS, 510, 131
Marini, I., Popesso, P., Lamer, G., et al. 2024, A&A, 689, A7
Marini, I., Popesso, P., Dolag, K., et al. 2025, A&A, 698, A191
Martizzi, D., Vogelsberger, M., Artale, M. C., et al. 2019, MNRAS, 486, 3766
Mernier, F., de Plaa, J., Kaastra, J. S., et al. 2017, A&A, 603, A80
Mirakhor, M. S., & Walker, S. A. 2020, MNRAS, 497, 3204
Mirakhor, M. S., Walker, S. A., & Runge, J. 2022, MNRAS, 509, 1109
Mohapatra, R., Jetti, M., Sharma, P., & Federrath, C. 2022, MNRAS, 510, 2327
Nagai, D., & Lau, E. T. 2011, ApJ, 731, L10
Nelson, D., Springel, V., Pillepich, A., et al. 2019, Comput. Astrophys. Cosmol., 6, 2
Nelson, D., Pillepich, A., Ayromlou, M., et al. 2024, A&A, 686, A157
Nevalainen, J., Lieu, R., Bonamente, M., & Lumb, D. 2003, ApJ, 584, 716
Nevalainen, J., Bonamente, M., & Kaastra, J. 2007, ApJ, 656, 733
Pillepich, A., Springel, V., Nelson, D., et al. 2018, MNRAS, 473, 4077
Planelles, S., Fabjan, D., Borgani, S., et al. 2017, MNRAS, 467, 3827
Plucinsky, P. P., Snowden, S. L., Briel, U. G., Hasinger, G., & Pfeffermann, E. 1993, ApJ, 418, 519
Power, C., Elahi, P. J., Welker, C., et al. 2020, MNRAS, 491, 3923
Rasia, E., Lau, E. T., Borgani, S., et al. 2014, ApJ, 791, 96
Reiprich, T. H., Veronica, A., Pacaud, F., et al. 2021, A&A, 647, A2
Rost, A., Kuchner, U., Welker, C., et al. 2021, MNRAS, 502, 714
Rost, A. M., Nuza, S. E., Stasyszyn, F., et al. 2024, MNRAS, 527, 1301
Rybicki, G. B., & Lightman, A. P. 1979, Radiative Processes in Astrophysics (New York: Wiley-Interscience)
Sakelliou, I., & Ponman, T. J. 2004, MNRAS, 351, 1439
Shi, X., Nagai, D., Aung, H., & Wetzel, A. 2020, MNRAS, 495, 784
Shreeram, S., Comparat, J., Merloni, A., et al. 2025a, A&A, 703, A137
Shreeram, S., Comparat, J., Merloni, A., et al. 2025b, A&A, 697, A22
Snowden, S. L., McCammon, D., Burrows, D. N., & Mendenhall, J. A. 1994, ApJ, 424, 714
Snowden, S. L., Freyberg, M. J., Plucinsky, P. P., et al. 1995, ApJ, 454, 643
Snowden, S. L., Egger, R., Freyberg, M. J., et al. 1997, ApJ, 485, 125
Tanimura, H., Aghanim, N., Douspis, M., & Malavasi, N. 2022, A&A, 667, A161
Tuominen, T., Nevalainen, J., Tempel, E., et al. 2021, A&A, 646, A156
Tuominen, T., Nevalainen, J., Heinämäki, P., et al. 2023, A&A, 671, A103
Vallés-Pérez, D., Planelles, S., & Quilis, V. 2021, MNRAS, 504, 510
Vogelsberger, M., Marinacci, F., Torrey, P., et al. 2018, MNRAS, 474, 2073
Voges, W., Aschenbach, B., Boller, T., et al. 1999, A&A, 349, 389
Vurm, I., Nevalainen, J., Hong, S. E., et al. 2023, A&A, 673, A62
Walker, S. A., Fabian, A. C., Sanders, J. S., George, M. R., & Tawara, Y. 2012, MNRAS, 422, 3503
Wang, W., Wang, P., Guo, H., et al. 2024, MNRAS, 532, 4604
Werner, N., Finoguenov, A., Kaastra, J. S., et al. 2008, A&A, 482, L29
Zappacosta, L., Maiolino, R., Mannucci, F., Gilli, R., & Schuecker, P. 2005, MNRAS, 357, 929
Zhang, C., Zhuravleva, I., Markevitch, M., et al. 2024a, MNRAS, 530, 4234
Zhang, X., Bulbul, E., Malavasi, N., et al. 2024b, A&A, 691, A234
Zhao, Y., Xu, H., Liu, A., et al. 2025, A&A, 695, A15